

Cite this: *J. Mater. Chem. A*, 2020, **8**, 2836

Insights into high capacity and ultrastable carbonaceous anodes for potassium-ion storage via a hierarchical heterostructure†

Chunrong Ma,^a Huijun Yang,^b Zhixin Xu,^c Zhengguang Fu,^d Yingying Xie,^e Hongti Zhang,^f Min Hong,^c ZiFeng Ma,^c Hui Xiong^b and Xian-Zheng Yuan^{*,a}

Carbonaceous materials are promising anode materials for potassium-ion batteries (PIBs). However, due to the large size of K^+ ions, pristine carbon anode materials exhibit poor rate capability and unsatisfactory cycling stability. Herein, a novel anode with a hierarchical porous carbon structure and defects is reported. Integrating the mesoporous structure and P-dopants at the carbon surface not only offers more active sites for K^+ adsorption but also enlarges the layer spacing to accommodate stress during potassiation/depotassiation. The as-prepared electrode exhibits ultrahigh stability at a current of 1 A g^{-1} (over 10 000 cycles without obvious capacity decay) and superior rate capability (165 mA h g^{-1} at a current density of 10 A g^{-1}), outperforming most of the reported carbonaceous electrodes in PIBs. Through integrated comprehensive experimental characterization and theoretical calculations, the charge storage and transport mechanisms in such a material demonstrate that P doping into the porous structure is beneficial for synergistically improving K^+ ion storage and transport by enhancing the adsorption of K^+ ions and reducing the diffusion barrier of K^+ ions. This work sheds light on how tailored heterostructures could enhance K^+ storage and transport and provide new pathways for materials design for ultrastable PIBs.

Received 27th November 2019
Accepted 9th January 2020

DOI: 10.1039/c9ta12997a

rsc.li/materials-a

Introduction

Over the past few decades, lithium-ion batteries (LIBs) have emerged as the most promising energy storage system and have attracted considerable attention due to their high power density and energy. Owing to the increasing development of smart power grids and automotive electric vehicle markets, the large-scale application of LIBs will face challenges such as limited lithium resources and high costs of raw materials in the foreseeable future.^{1–3} Therefore, exploring next-generation alternative batteries based on abundant metals (*e.g.*, Na, K, Al, Mg, and

Ca) is important to ensure long-term and sustainable energy development. Among these candidates, potassium-ion batteries (PIBs) are attracting increasing attention because of the high abundance of potassium ions and the low redox potential of K^+/K (-2.93 V vs. the standard hydrogen electrode), which is close to that of Li^+/Li (-3.04 V).^{4–6} Considering the similarity between the operating mechanisms of KIBs and LIBs, carbon-based anode materials are expected to be the most promising materials for practical applications due to their availability and low cost. However, carbon anodes have a few hurdles in realizing their practical applications in PIBs. For instance, the ordered and layered graphite materials deliver a theoretical capacity of only 279 mA h g^{-1} (KC_8) in KIBs, which is less than that of their analogs in LIBs (LiC_6 ; 372 mA h g^{-1}). Additionally, the radius of the K^+ ion is larger than that of the Li^+ ion; therefore, graphite does not easily accommodate fast insertion and extraction of K^+ ions into its small interlayers through intercalation. Recently, a series of modified carbon structures, such as soft-hard carbon, soft carbon, and mesoporous carbon were used as PIB anodes.^{7–9} Although some enhancement is observed, the practical rate capacity and cycling stability are still well below the expectation for high power and high energy PIBs, owing to the poor diffusion kinetics of large K^+ ions.

To overcome the aforementioned limitations, the key is adjusting the electronic structure and morphology of carbon materials to enhance K^+ diffusion, *i.e.*, decreasing the diffusion

^aShandong Key Laboratory of Water Pollution Control and Resource Reuse, School of Environmental Science and Engineering, Shandong University, Qingdao, 266237, China. E-mail: xzyuan@sdu.edu.cn

^bEnergy Technology Research Institute, National Institute of Advanced Industrial Science and Technology (AIST), Tsukuba, 305-8568, Japan

^cShanghai Electrochemical Energy Devices Research Centre, School of Chemistry and Chemical Engineering, Shanghai Jiao Tong University, Shanghai, 200240, China

^dQingdao Institute of Bioenergy and Bioprocess Technology, Chinese Academy of Sciences, Qingdao, 266101, China

^eMicron School of Materials Science and Engineering, Boise State University, Boise, ID 83725, USA

^fSchool of Physical Science and Technology, Shanghai Tech University, Shanghai 201210, China

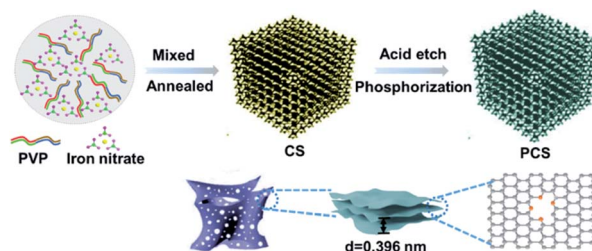
† Electronic supplementary information (ESI) available. See DOI: 10.1039/c9ta12997a

barrier to accelerate the ion/electron transport and enlarging the interlayer spacing to accommodate the volume expansion. A porous network is advantageous to shorten the ion diffusion path and provide more active sites for enhancing the adsorption kinetics.¹⁰ Heteroatom doping as an efficient approach has been proven to be beneficial for tuning the electrochemical and physicochemical properties of carbon materials.^{11–13} Zhang *et al.* reported a hierarchically porous nitrogen-doped carbon electrode for potassium ion batteries through both electrochemical and computational approaches, which utilized N doping to optimize its electronic structure to promote charge transport, thereby enhancing its performance.¹⁴ In comparison with N and other dopants, P, as the most stable chemisorption-type dopant, promotes out-of-plane puckering of defect sites and has been shown to enable faster charge transfer in SIBs.¹⁵ Hence, introducing P into a porous carbon structure could be a promising strategy to create more active sites and accelerate charge transfer. Nevertheless, detailed mechanisms regarding P-doping into porous carbon for PIBs have seldom been reported, and other fundamental properties, such as the ion/electron diffusion, electronic structure, crystal phase change, and compositional evolution of the host material during potassiation/depotassiation, remain unclear. Therefore, the development of a rational design procedure utilizing novel porous structures with P doping is critical to comprehensively understand and elucidate its electrochemical behavior in PIBs, which could provide insights into the design rules for other advanced anode materials for PIBs.

Herein, we report three-dimensional (3D) P-doped porous carbon nanosheets (PCSSs) with a high specific surface area, abundant pore structure, expanded interlayer space, and superior electronic structure. The superior interconnected 3D porous structure along with P-doping can not only optimize the equilibrium state of electrons to improve the mobility of K^+ ions/electrons but also create more active sites to enhance the surface-capacitive charge storage. Benefiting from the unique morphology and additional P doping, the prepared PCSSs delivered high specific capacity, excellent rate capability (165 mA h g^{-1} at 10 A g^{-1}) and superior cycling performance (over 10 000 cycles at 1 A g^{-1} without obvious capacity fading). The underlying charge storage mechanism for the PCSSs is elucidated *via* kinetics analysis, *in situ* X-ray diffraction (XRD), *ex situ* X-ray photoelectron spectroscopy (XPS), and theoretical calculations. The results showed that P doping is beneficial to synergistically improve the electrochemical performance by enhancing the adsorption of K^+ ions and reducing their diffusion barrier. Moreover, the 3D porous structure promotes fast electron transfer and fast K^+ ion diffusion. This work not only offers new insights into electrode materials for structural design in PIBs but also provides a fundamental understanding of the role of heteroatoms in the K^+ ion storage mechanism.

Results and discussion

The PCSSs were fabricated *via* melt nitrate-assisted chemical blowing, and the preparation process is illustrated in Scheme 1. Specifically, Fe-decorated porous carbon was first produced *via*



Scheme 1 Synthesis of PCSSs and a sketch of their structure.

carbonization of polyvinylpyrrolidone (PVP) with assistance from iron(III) nitrate. The homogeneous mixture of PVP and iron(III) nitrate gradually formed a viscous gel when heated and exhibited a strong binding between the metal cations and PVP. When the sintering temperature was increased, the gel expanded to form a loose and bubble-like structure *via* the production of gas bubbles due to the decomposition of iron(III) nitrate and was subsequently carbonized into cross-linked carbon sheets.¹⁶ Simultaneously, the Fe species were formed *in situ* and embedded in the carbon matrix by the carbothermal reduction of iron oxides at higher temperatures. The Fe nanoparticles were then etched from the porous carbon by treatment with HCl, which introduced abundant nanosized pores into the carbon sheets. Finally, the porous carbon was treated by phosphorization to introduce the P dopant. For comparison, the undoped porous carbon structure was prepared using a similar process (CSs). The morphology and structures of CSs and PCSSs were characterized *via* scanning electron microscopy (SEM) and high-resolution transmission electron microscopy (HRTEM), as shown in Fig. 1. CSs exhibit a foam-like structure with linked macropores with a diameter of 1–3 μm as observed by SEM (Fig. 1a). After phosphorization, the PCSSs (Fig. 1b) inherit the well-developed porous structure of CSs and exhibit a similar 3D structure. The SEM image in Fig. 1c reveals that the macropore walls are comprised of connected carbon nanosheets with a large in-plane size of several micrometers, and the thickness of the carbon walls ranges from 10 to 20 nm. The interconnected conductive carbon framework can facilitate fast electron transport.^{17,18} TEM characterization was used to further explore the structure of the PCSSs (Fig. 1d and S2†). Distinct large

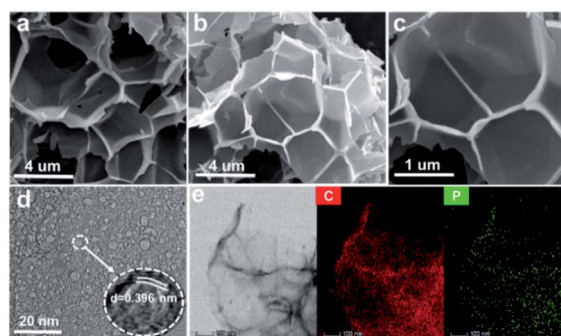


Fig. 1 SEM images of (a) CSs and (b, c) PCSSs. (d) TEM image of PCSSs (inset: HRTEM). (e) STEM mapping images of PCSSs.

nanopores with an average diameter of approximately 5 nm are uniformly dispersed on the ultra-thin carbon sheets and are well consistent with the embedded Fe nanoparticles (Fig. S1†). The nanopores could not only accommodate the volume change during potassiation/depotassiation but also offer more active sites to adsorb K^+ . From the high-resolution TEM (HRTEM) image, lattice fringes with a 0.396 nm spacing were observed, which is larger than that of graphitic carbon (0.335 nm) and ensures the convenient intercalation of K^+ (Fig. 1d inset). Moreover, the scanning transmission electron microscopy (STEM) mapping analysis (Fig. 1e) demonstrates that the P element is homogeneously distributed in the carbon matrix.

XRD analysis and Raman spectroscopy were performed to further explore the microstructure of PCSs. The XRD pattern of PCSs (Fig. 2a) shows a broad peak at 23.2° while that of CSs shows a peak at 25.8° ; these peaks were indexed to the (002) plane. Compared with the (002) CS peak, the PCS peak shifts to a smaller angle, which indicates a larger interlayer spacing resulting from the introduction of P.¹⁹ The interlayer spacing of PCSs was calculated to be 0.396 nm, in accordance with HRTEM observations. The Raman spectra (Fig. 2b) exhibited two distinct peaks at 1337 and 1584 cm^{-1} , corresponding to the D band (disordered carbon) and G band (in-plane vibrational sp^2 carbon), respectively.²⁰ The defective and graphitic structure can be described using I_D/I_G . The I_D/I_G value of PCSs (0.99) is larger than that of CSs (0.78), which is attributed to the greater number of defects in PCSs due to P doping.²¹ These defects can increase the number of active sites to accommodate more K^+ , thereby promoting energy storage. The surface chemical state of PCSs was further evaluated by XPS. From the survey spectra (Fig. 2c), both C and P signals were detected in the PCSs, whereas only the C signal was detected in the CSs, confirming that P was successfully introduced into PCSs. The content of P was 4.32%.

In addition, in the P 2p high-resolution spectrum (Fig. 2d), the P main peak can be deconvoluted into two peaks: the peak

at a binding energy of 134.4 eV is ascribed to P–O with a high oxidation state of P, which can be attributed to the surface oxidized P species, whereas that at 133.1 eV is attributed to P–C bonds. Based on the XPS results, it can be concluded that the P atom was incorporated into the carbon by covalent bonding. In addition, in the C 1s high-resolution spectrum (Fig. S4†), the three fitted peaks at binding energies of 284.8, 285.9, and 288.9 eV are indexed to C–C, C–O–C, and O–C=O, respectively.

The surface area of PCSs was analyzed using N_2 adsorption–desorption isotherms, as shown in Fig. 2e. An isotherm with a typical H4-type hysteresis loop is distinctly observed, illustrating that both micropores and mesopores exist in the PCSs.²² In addition, the Brunauer–Emmett–Teller specific surface area based on the isotherm was calculated to be $783\text{ m}^2\text{ g}^{-1}$, which is close to that of the CSs ($716\text{ m}^2\text{ g}^{-1}$). The average pore size distribution is illustrated in Fig. 2f, where the pores contain micropores and mesopores centered from 0.58 to 20 nm. Two peaks were dominant in the size range below 2 nm, which were attributed to the defect sites introduced by P doping,²³ while mesopores mainly centered at 2–5 nm due to the corrosion of Fe nanoparticles. Such a large specific area and pore structure could promote ion/electron transport leading to high electrochemical performance. Also, the density of the PCSs is found to be 0.63 g cm^{-3} using a digital density analyzer (JW-M100). The introduction of phosphorus can significantly improve the electrical conductivity of graphene. Compared to CSs, PCSs demonstrate a remarkable increase in electrical conductivity by up to 2 orders of magnitude (36 S m^{-1}), facilitating fast electron transport.

The K^+ storage properties of PCSs were first evaluated by cyclic voltammetry (CV) using half-cells with a potassium plate as the counter electrode. As shown in Fig. 3a, the CV curves of PCSs were recorded at a scan rate of 0.1 mV s^{-1} within a potential window from 0.01 to 2.5 V. The predominant peak at 0.78 V in the initial cathodic process is distinctly different from the peaks in subsequent cycles, which indicates the formation

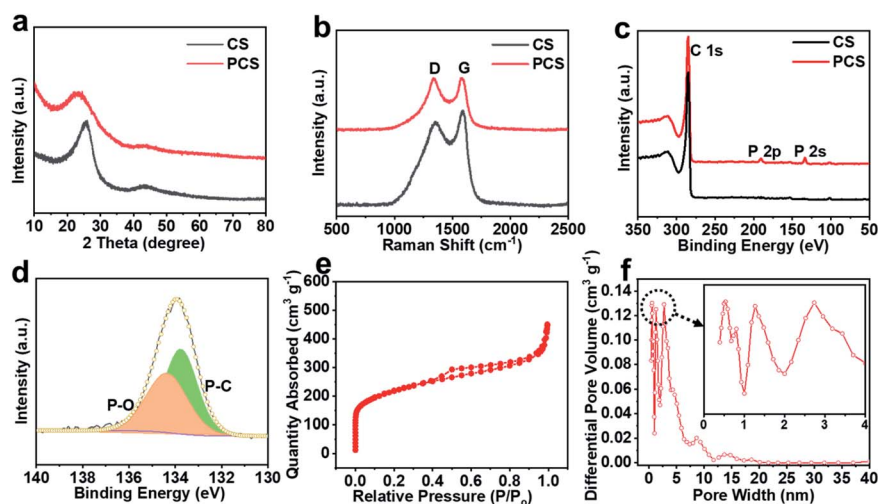


Fig. 2 (a) XRD patterns, (b) Raman spectra, and (c) XPS survey spectra of CSs and PCSs. (d) High-resolution P spectrum of PCSs. (e) N_2 adsorption–desorption isotherm and (f) pore size distribution of PCSs.

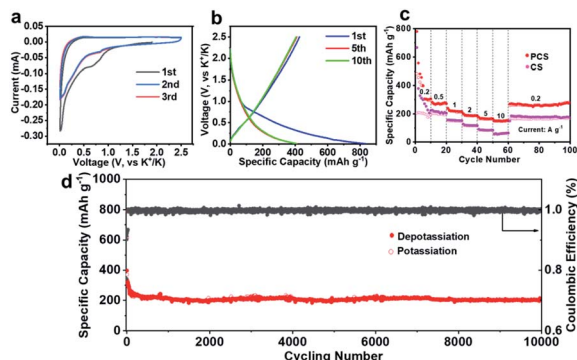


Fig. 3 Electrochemical performance of PCS and CS electrodes as anodes for PIBs. (a) CV curves of PCSs from 0.01 to 2.5 V at a scan rate of 0.1 mV s^{-1} ; (b) charge–discharge profiles of PCSs within a potential window of 0.01–2.5 V; (c) rate capability of PCSs and CSs; (d) long-term cycling performance of a PCS electrode at a current of 1 A g^{-1} .

of a solid electrolyte interphase (SEI) layer in the first cycle.^{24,25} Meanwhile, a sharp peak appeared at approximately 0.105 V, which is attributed to insertion of K^+ into the interlayers of PCSs in the form of a K-intercalated compound.²⁶ Accordingly, the broad peak at 0.4 V in the anodic process is related to the deintercalation of K^+ . During the subsequent cycles, CV curves almost overlap between the second and third cycles, suggesting good reversibility. The charge–discharge profiles of the PCS electrode at a current of 100 mA g^{-1} are shown in Fig. 3b. The initial discharge and charge specific capacity were 805 and 436 mA h g^{-1} , respectively, corresponding to an initial coulombic efficiency (ICE) of 54%. The large irreversible capacity and relatively low ICE can be associated with the large consumption of the electrolyte during the formation of the SEI in the initial cycle due to the large surface area.²⁷ Moreover, the porous structure could lead to a low electrode packing density ($\sim 0.16 \text{ g cm}^{-3}$) and volumetric capacity ($\sim 55 \text{ A h L}^{-1}$), which present challenges for practical applications of PIBs. Guo *et al.* reported that well-mixed nano- and micro-sized materials may achieve a balance between the energy density and power density, which inspired us to conduct further studies for engineering high energy materials in our current work.²⁸ Interestingly, the PCS electrode exhibited a better ICE than the CS electrode (Fig. S5†) and other reported porous carbon structures.^{23,24,26,29–31} The enhanced ICE can be attributed to the P doping. Owing to the larger size, P is more likely to dope the carbon at the edge-plane sites, which can possibly lead to less trapped K^+ , improving the ICE.³² After several cycles, the CE increased to $\sim 100\%$ and the electrode demonstrated a reversible capacity. Furthermore, the discharge profile of PCSs exhibited a sloping feature without an obvious plateau at voltages above 0.1 V, indicating a single solid solution behavior.³³ The rate capability of the PCS electrode with current densities from 0.2 to 10 A g^{-1} is shown in Fig. 3c. The PCS electrode delivered a discharge capacity of 285 mA h g^{-1} at a current density of 0.5 A g^{-1} . When the current increased gradually, discharge capacities of 232, 203, and 174 mA h g^{-1} were reached at current densities of 1, 2, and 5 A g^{-1} , respectively.

Remarkably, even at a high current density of 10 A g^{-1} , a high capacity of 165 mA h g^{-1} was still obtained. Furthermore, the capacity recovered to 302 mA h g^{-1} when the current density was ramped back to 0.2 A g^{-1} . The nearly negligible capacity loss after deep charge–discharge cycles at a high current density further illustrates the great structural stability within the electrode. Meanwhile, the undoped CS electrode was evaluated as a control; a discharge capacity of 50 mA h g^{-1} was delivered at 10 A g^{-1} , which is only one-third the capacity of the PCS electrode. Long-term cycling stability is an important target in appraising K^+ storage performance. However, the insertion/extraction of K^+ in carbon was severely hampered by the larger size of K^+ compared to Na^+ and Li^+ . In addition, the stress along with the volume change during the repeated charge/discharge process could destroy the structural stability of the carbon materials. The long-term cycling performance of the PCS electrode was evaluated at a high current density of 1 A g^{-1} , as shown in Fig. 3d. Notably, even after 10 000 cycles, the PCS electrode could still maintain a capacity of 201 mA h g^{-1} , showing no obvious capacity fading. Furthermore, the CE increased to ~ 99 – 99.8% after the initial cycles and was maintained over the subsequent long-term cycling process. This excellent electrochemical performance of PCSs in terms of high specific capacity, rate capability, and cycling stability makes it very attractive as a potential anode for high-power PIBs (the rate and cycling stability of the PCSs in the present work are compared with those reported in the literature in Table S1,† and they surpass those of most of the reported carbonaceous electrodes in PIBs).

To elucidate the charge storage mechanism, kinetics analysis was carried out by CV at various scan rates. Fig. 4a shows the CV curves at various scan rates from 0.1 to 2 mV s^{-1} ; the CV curves at different scan rates have similar shapes without discernable redox peaks. It is assumed that a relationship exists between measured current (i) and scan rate (v):³⁴

$$i = av^b \quad (1)$$

where a and b are adjustable parameters, and b can be obtained from the slopes of the $\log(v) - \log(i)$ plots. The b value varies

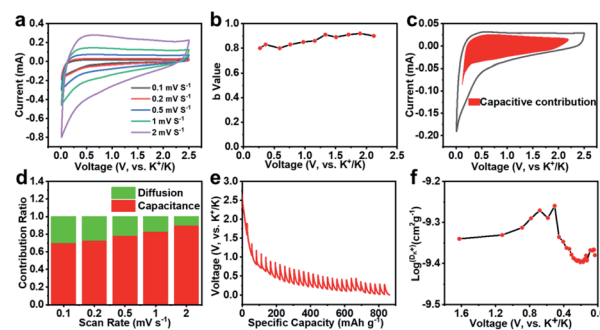


Fig. 4 (a) CV curves recorded at different scan rates. (b) b values and voltammetric responses (0.1 mV s^{-1}). (c) Capacitive contribution to the overall cyclic voltammetry response at 0.1 mV s^{-1} . (d) Capacitive ratio at various scan rates from 0.1 to 2 mV s^{-1} . (e) GITT profile and (f) the D_{K^+} coefficients calculated from the GITT profiles of the PCS electrode.

from 0.5 to 1; specifically, when b equals 0.5, diffusion contributes to the total current, whereas when b reaches 1, the capacitive behavior dominates the whole reaction process.^{35,36} The b values at different potentials were calculated (Fig. 4b).

The b values during the cathodic process were mostly greater than 0.8, suggesting that the overall charge storage was mainly from the surface-capacitive processes, which promote fast kinetics. The typical double-layer capacitance is substantially smaller than the estimated surface-area-normalized capacitance, which indicates that the K^+ storage on the surface is associated with pseudocapacitive behavior. The capacitive contribution at a given scan rate can be distinguished and separated from the fixed behaviors through the following equation:³⁷

$$i = k_1 v + k_2 v^{1/2} \quad (2)$$

By calculating k_1 , the surface capacitive effect can be distinctly distinguished. As illustrated in Fig. 4c, the capacitive contribution accounts for 68% of the whole charge at 0.1 $mV s^{-1}$, and the diffusion effect is only localized when the potential is approximately equal to 0 V. Furthermore, this proportion increases with an increase in the scan rate, reaching 91% at 2 $mV s^{-1}$ (Fig. 4d). The high capacitive contribution to charge storage of the PCS electrode indicates that the defect sites created by the P doping and porous structure play a substantial role in the fast kinetics and enhanced K^+ adsorption, which lead to superior rate capability.

The galvanostatic intermittent titration technique (GITT) was carried out to obtain information regarding diffusion of K^+ in the PCS electrode. Fig. 4e shows the GITT curve obtained by applying a series of current pulses at 100 $mA g^{-1}$ for 0.5 h followed by a 2 h relaxation process. The change in potential during relaxation corresponds to the rate of K^+ diffusion (D_{K^+}). The D_{K^+} value can be quantified on the basis of the following equation (Fig. S6[†]):³⁸

$$D_{K^+} = \frac{4}{\pi} \left(\frac{m_B V_M}{M_B A} \right)^2 \left(\frac{\Delta E_s}{\Delta E_t} \right)^2 (\tau \ll L^2 / D_{K^+}) \quad (3)$$

The calculated D_{K^+} value during the discharge process is shown in Fig. 4f. The D_{K^+} of PCSs is substantially higher than that of CSs (Fig. S7[†]), indicating faster diffusion in PCSs. Because of the P doping, the expanded interlayer space has the potential to accommodate more K^+ and adapt to the interlayer spacing change during the charge–discharge processes.³⁹ *In situ* XRD characterization was used to investigate the structural evolution of PCSs during the potassiation/depotassiation process. The evolution of the (002) peak of the PCS electrode at 100 $mA g^{-1}$ in the first cycle within the voltage window from 0.01 to 2.5 V is shown in Fig. 5a. In the pristine state, the peak was located at 23.2°, which is consistent with the *ex situ* XRD results (Fig. 2a). In the initial period (>0.2 V), the (002) peak exhibited no obvious change in either position or shape, indicating that K^+ adsorption is predominant in this region. Because of the numerous defect sites on the carbon surface and the porous structure, large amounts of K^+ will be adsorbed and

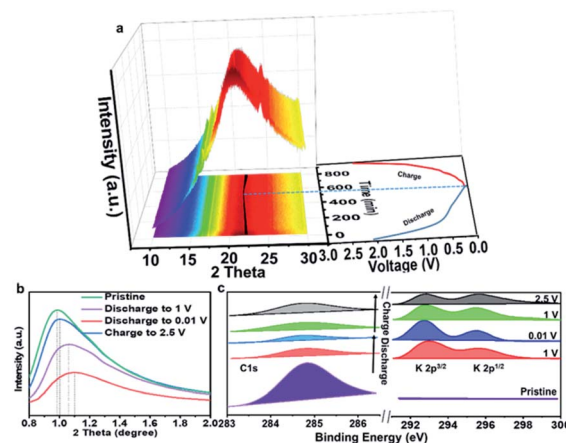


Fig. 5 (a) *In situ* XRD patterns of a PCS electrode at voltages ranging from 0.01 to 2.5 V. (b) *Ex situ* small angle X-ray scattering patterns and (c) XPS spectra of a PCS electrode at different potassiation states.

the adsorption on the active sites will not directly affect the structural integrity. These results are consistent with the aforementioned kinetic analysis showing that the K^+ storage is mainly from adsorption in the sloping region. Upon further potassiation and below 0.2 V, the diffraction peak of (002) shifted to a lower angle and reached its maximum at 0.01 V. Meanwhile, the peak broadened and was slightly compressed, which is reasonable because intercalation of K^+ in the carbon anode leads to the expansion of interlayer spacing and increased disorder. Interestingly, the (002) peak position and intensity recovered when scanned anodically from 0.01 to 2.5 V, indicating contraction of the interlayer distance and recovery from the disordered structure accompanying K^+ extraction. Notably, the (002) peak did not completely return to its initial position after the cell was fully charged to 2.5 V, illustrating the possible remaining swelling of turbostratic galleries in the PCS electrode in the first cycle due to some trapped K^+ .⁴⁰ This result is consistent with the result of ICE indicating the trapping of some irreversible K^+ in the carbon layer apart from the formation of SEI.

Ex situ small angle X-ray scattering of the PCSs at various states of charge was performed (Fig. 5b). The scattering peak shifted to a larger angle from the pristine state to 0.01 V during the discharge process. When the electrode was switched to the depotassiation state (to 2.5 V), the peak shifted backward but could not go back to its pristine state. During the discharge process, K^+ was adsorbed onto the mesopores of the surface and partially filled the mesopores. With the depotassiation process, the K^+ began to desorb from the PCS electrode. Meanwhile, the mesopores were recovered but could not return to their original size completely, indicating that trace amounts of K^+ remained in the PCS electrode.⁴¹ Such results are consistent with the *in situ* XRD results and confirm that the K^+ is successfully inserted/extracted into/from the PCS electrode. The *ex situ* XPS spectra acquired at different charge/discharge states were used to further investigate the compositional variation during the potassiation/depotassiation process of the PCS electrode

(Fig. 5c). The C 1s peak exhibited a distinct reversible change during the whole process, demonstrating the formation of potassium–carbon compounds. The K peaks were not detected in the spectrum of the as-prepared electrode before potassiation. However, upon potassiation, the K 2p peak appeared with an increased intensity that reached a maximum at 0.01 V. This observation indicates that K^+ is present in the electrode and that the quantity is increased when accompanied by potassiation.³⁹ Subsequently, the K 2p peak becomes weak in the potassiation process; however, the weak K 2p peak could still be observed until the electrode was charged to 2.5 V. This indicates that K^+ cannot be extracted completely from the potassium–carbon compounds after the first cycle.

To better comprehend in-depth the origin of K^+ storage and the role of P doping in K^+ adsorption and the electronic properties of the PCS electrode, DFT-based first-principles calculations were conducted. For comparison, the adsorption energies (ΔE) of ideal graphene and the defective graphene without P doping were also calculated. On the basis of three different carbon structure models with K adsorbed at corresponding sites (Fig. 6a–c), the related ΔE of PCSs was obtained (-2.83 eV) and found to be greater than those of graphene (-0.38 eV) and defect-introduced graphene (-1.52 eV). These results demonstrate that the PCSs have the strongest K^+ adsorption ability because of the electron-rich structure through P doping, which plays a significant role in explaining the enhanced capacity.⁴² Therefore, increasing the P content is a necessary way to improve the capacity of carbon-based materials. Furthermore, the density of states (DOS) on ideal graphene, defect-introduced graphene, and a PCS structure was explored, as shown in Fig. 6d. Compared with that of the graphene and defect-introduced graphene, the DOS of PCSs shows a metallic state upon introduction of P doping and the compound retains its metallic character even after it adsorbs K^+ . This result illustrates the high electron mobility, which cannot be controlled by the electron transport kinetics. The rate capability is generally accepted as being associated with ion transport and electron

transport kinetics. According to the aforementioned calculations, the PCSs demonstrate superior rate capability and a high specific capacity as a potential anode material for PIBs.

Conclusions

In summary, we demonstrated a mesoporous PCS electrode with controlled P-doping as a novel anode for PIBs. The outstanding electrochemical performance of PCSs was understood through integrated experimental and theoretical analysis including *in situ* XRD, *ex situ* SIXS and XPS, CV, GITT, and DFT calculations. The results demonstrated that the K^+ storage capacity was mainly from the sloping region, which can be associated with defects/pores for K^+ adsorption/desorption rather than intercalation, leading to improved kinetics and cycling stability. Kinetics analysis showed that more than 90% storage contribution was from the surface-driven behavior, which can facilitate fast charge transport and structural stability. Moreover, the GITT revealed a higher K^+ diffusion coefficient for PCSs than for CSs due to the well-designed pore structure and P-doping. The compositional/structural evolution tests confirmed that K^+ could be reversibly intercalated/deintercalated into/from the PCSs, which is a prerequisite for achieving high specific capacity and long-term stability. DFT calculations were further performed to demonstrate the important role of P doping in the carbon structure—specifically, that P doping can enhance the mobility of K^+ , thereby ensuring superior rate capability and high K^+ storage capacity. This elucidation of the K^+ storage mechanisms offers a new path to design anode materials with excellent performance in PIBs by optimizing the electronic structure to realize high power density and energy density.

Conflicts of interest

There are no conflicts to declare.

Acknowledgements

This work was supported by the National Basic Research Program of China (2014CB239700) and the National Natural Science Foundation of China (2190516, 21336003, and 21676165). The author thank Xiaojun Li from State Key Laboratory of Microbial Technology, Shandong University for the assistance in transmission electron microscope.

Notes and references

- 1 L. Zhang, S. Peng, Y. Ding, X. Guo, Y. Qian, H. Celio, G. He and G. Yu, *Energy Environ. Sci.*, 2019, **12**, 1989–1998.
- 2 G. Li, B. Huang, Z. Pan, X. Su, Z. Shao and L. An, *Energy Environ. Sci.*, 2019, **12**, 2030–2053.
- 3 J. Peters, D. Buchholz, S. Passerini and M. Weil, *Energy Environ. Sci.*, 2016, **9**, 1744–1751.
- 4 J. Wang, L. Fan, Z. Liu, S. Chen, Q. Zhang, L. Wang, H. Yang, X. Yu and B. Lu, *ACS Nano*, 2019, **13**, 3703–3713.

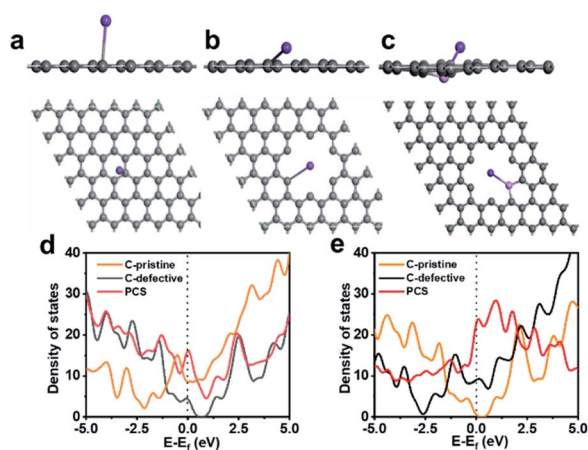


Fig. 6 The first principles calculation models. Side and top views of (a) the C-pristine, (b) C-defective, and (c) the PCS carbon structure. (d and e) Corresponding DOS before and after potassiation.

- 5 Y. An, Y. Tian, L. Ci, S. Xiong, J. Feng and Y. Qian, *ACS Nano*, 2018, **12**, 12932–12940.
- 6 J. Chu, W. A. Wang, J. Feng, C.-Y. Lao, K. Xi, L. Xing, K. Han, Q. Li, L. Song, P. Li, X. Li and Y. Bao, *ACS Nano*, 2019, **13**, 6906–6916.
- 7 X. Yao, Y. Ke, W. Ren, X. Wang, F. Xiong, W. Yang, M. Qin, Q. Li and L. Mai, *Adv. Energy Mater.*, 2019, **9**, 1803260.
- 8 X. Zhou, L. Chen, W. Zhang, J. Wang, Z. Liu, S. Zeng, R. Xu, Y. Wu, S. Ye, Y. Feng, X. Cheng, Z. Peng, X. Li and Y. Yu, *Nano Lett.*, 2019, **19**, 4965–4973.
- 9 Z. Liu, J. Wang, X. Jia, W. Li, Q. Zhang, L. Fan, H. Ding, H. Yang, X. Yu, X. Li and B. Lu, *ACS Nano*, 2019, **13**, 10631–10642.
- 10 Y. Wang, Z. Wang, Y. Chen, H. Zhang, M. Yousaf, H. Wu, M. Zou, A. Cao and R. Han, *Adv. Mater.*, 2018, **30**, 1802074.
- 11 B. Li, B. xi, F. Wu, H. Mao, J. Liu, J. Feng and S. Xiong, *Adv. Energy Mater.*, 2018, **9**, 1803070.
- 12 Y. Guo, W. Liu, R. Wu, L. Sun and B. Shan, *ACS Appl. Mater. Interfaces*, 2018, **10**, 14304.
- 13 G. Zou, H. Hou, G. Zhao, Z. Huang, G. Peng, X. Ji, G. Zou, H. Hou, G. Zhao and Z. Huang, *Green Chem.*, 2017, **19**, 10–1039.
- 14 C. Chen, Z. Wang, B. Zhang, L. Miao, J. Cai, L. Peng, Y. Huang, J. Jiang, Y. Huang, L. Zhang and J. Xie, *Energy Storage Materials*, 2017, **8**, 161–168.
- 15 Y. Yang, D. M. Tang, C. Zhang, Y. Zhang, Q. Liang, S. Chen, Q. Weng, M. Zhou, Y. Xue and J. Liu, *Energy Environ. Sci.*, 2017, **10**, 979–986.
- 16 Z. Schnepf, M. Thomas, S. Glatzel, K. Schlichte, R. Palkovits and C. Giordano, *J. Mater. Chem.*, 2011, **21**, 17760–17764.
- 17 B. Cao, H. Liu, B. Xu, Y. Lei, X. Chen and H. Song, *J. Mater. Chem. A*, 2016, **4**, 6472–6478.
- 18 F. Zhang, T. Liu, M. Li, M. Yu, Y. Luo, Y. Tong and Y. Li, *Nano Lett.*, 2017, **17**, 3097.
- 19 E. Hao, L. Wei, L. Shuang, Z. Yuan, H. Wang, S. Chen, F. Cheng, S. Zhao and H. Yang, *J. Mater. Chem. A*, 2016, **5**, 2204–2214.
- 20 W. Hui, S. Kai, T. Franklin, D. J. Stacchiola and H. Yun Hang, *Angew. Chem., Int. Ed.*, 2013, **52**, 9210–9214.
- 21 W. Yang, J. Zhou, S. Wang, W. Zhang and S. Guo, *Energy Environ. Sci.*, 2019, **12**, 1605–1612.
- 22 X. Gao, J. Feng, D. Su, Y. Ma, G. Wang, H. Ma and J. Zhang, *Nano Energy*, 2019, **59**, 598–609.
- 23 H. Li, Z. Cheng, Q. Zhang, A. Natan, Y. Yang, D. Cao and H. Zhu, *Nano Lett.*, 2018, **18**, 7407–7413.
- 24 X. Wang, K. Han, D. Qin, Q. Li, C. Wang, C. Niu and L. Mai, *Nanoscale*, 2017, **9**, 18216.
- 25 L. Lei, C. Yu, Y. Xie, T. Peng, Q. Li and C. Yan, *Adv. Funct. Mater.*, 2018, 1801989.
- 26 M. Chen, W. Wang, X. Liang, S. Gong, J. Liu, Q. Wang, S. Guo and H. Yang, *Adv. Energy Mater.*, 2018, **8**, 1800171.
- 27 Y. Li, C. Yang, F. Zheng, X. Ou, Q. Pan, Y. Liu and G. Wang, *J. Mater. Chem. A*, 2018, **6**, 17959.
- 28 W. Zhang, Y. Liu and P. Guo, *Sci. Adv.*, 2019, **5**, eaav7412.
- 29 D. Li, X. Ren, Q. Ai, Q. Sun, L. Zhu, Y. Liu, Z. Liang, R. Peng, P. Si, J. Lou, J. Feng and L. Ci, *Adv. Energy Mater.*, 2018, **8**, 1802386.
- 30 D. Liu, X. Huang, D. Qu, D. Zheng, G. Wang, J. Harris, J. Si, T. Ding, J. Chen and D. Qu, *Nano Energy*, 2018, **52**, 1–10.
- 31 C. Gao, Q. Wang, S. Luo, Z. Wang, Y. Zhang, Y. Liu, A. Hao and R. Guo, *J. Power Sources*, 2019, **415**, 165–171.
- 32 C. Ma, C. Deng, X. Liao, Y. He, Z. Ma and H. Xiong, *ACS Appl. Mater. Interfaces*, 2018, **10**, 36969–36975.
- 33 W. Wang, J. Zhou, Z. Wang, L. Zhao, P. Li, Y. Yang, C. Yang, H. Huang and S. Guo, *Adv. Energy Mater.*, 2018, **8**, 1701648.
- 34 J. Wang, J. Polleux, J. Lim and B. Dunn, *J. Phys. Chem. C*, 2007, **111**, 14925–14931.
- 35 C. Chen, Y. Wen, X. Hu, X. Ji, M. Yan, L. Mai, P. Hu, B. Shan and Y. Huang, *Nat. Commun.*, 2015, **6**, 6929.
- 36 D. Chao, C. Zhu, P. Yang, X. Xia, J. Liu, J. Wang, X. Fan, S. V. Savilov, J. Lin, H. J. Fan and Z. X. Shen, *Nat. Commun.*, 2016, **7**, 12122.
- 37 T. C. Liu, W. G. Pell, B. E. Conway and S. L. Roberson, *J. Electrochem. Soc.*, 1998, **145**, 1882–1888.
- 38 Y. Li, Y.-S. Hu, X. Qi, X. Rong, H. Li, X. Huang and L. Chen, *Energy Storage Materials*, 2016, **5**, 191–197.
- 39 L. Liu, Y. Chen, Y. Xie, P. Tao, Q. Li and C. Yan, *Adv. Funct. Mater.*, 2018, **28**, 1801989.
- 40 S. Qiu, L. Xiao, M. L. Sushko, K. S. Han, Y. Shao, M. Yan, X. Liang, L. Mai, J. Feng, Y. Cao, X. Ai, H. Yang and J. Liu, *Adv. Energy Mater.*, 2017, **7**, 1700403.
- 41 D. A. Stevens and J. R. Dahn, *J. Electrochem. Soc.*, 2001, **148**, A803–A811.
- 42 H. He, D. Huang, Y. Tang, Q. Wang, X. Ji, H. Wang and Z. Guo, *Nano Energy*, 2019, **57**, 728–736.